Electronic Supplementary Information

Heat dissipation effects on the stability of planar perovskite solar cells

Kyoungwon Choi,‡ Junwoo Lee,‡ Hyuntae Choi, Guan-Woo Kim, Hong Il Kim* and Taiho Park*

[*] Corresponding author

E-mail: hongilkim@postech.ac.kr (H. I. Kim); taihopark@postech.ac.kr (T. Park)

[‡] These authors contributed equally to this work.

Department of Chemical Engineering, Pohang University of Science and Technology (POSTECH), 77 Cheongam-Ro, Nam-gu, Pohang, Gyeongbuk 37673, Republic of Korea.

Fax: +82-54-279-8298; Tel: +82-54-279-2394

This file includes:

Experimental details

Materials

Cesium iodide (CsI), Sn(II) chloride dihydrate ($SnCl_2 \cdot 2H_2O$), 4-*tert*-butylpyridine (*t*BP), bis(trifluoromethane) sulfonimide lithium salt (Li-TFSI), Zinc powder, acetone (Ace), hydrochloric acid (HCl), chlorobenzene (CB), 2-methylanisole (2MA), ethanol (EtOH), acetonitrile (AN), isopropanol (IPA), dimethylformamide (DMF), dimethyl sulfoxide (DMSO) and aluminum oxide (Al_2O_3) were purchased from Sigma-Aldrich; formamidinium iodide (FAI), methylammonium bromide (MABr), and cobalt(III) tris(bis(trifluoromethyl-sulfonyl)imide) (FK209) were purchased from GreatCell Solar; lead(II) iodide (PbI_2) and lead(II) bromide ($PbBr_2$) were purchased from TCI. Spiro-OMeTAD was purchased from 1-Material.

Device fabrication

Perovskite solar cells were fabricated onto a fluorine-doped tin oxide (FTO) glass (HS Technologies, Resistivity L < 8 Ω). Some parts of the FTO were etched with zinc powder and 2 M HCl solution. The FTO was sonicated for 10 min using deionized water (DI-water), EtOH, Ace, and IPA. The organic residues on the etched FTO were removed by UV ozone treatment for 15 min. A SnO_2 electron transport layer with a solution of 0.1 M Sn(II) chloride dihydrate ($SnCl_2 \cdot 2H_2O$) in EtOH was spin-coated at 2,000 rpm for 30 s and then annealed at 180 °C for 1 hour. Zwitterion solution was coated on SnO_2 layer at 5,000 rpm for 60 s and annealed at 100 °C for 10 min. Perovskite precursors were prepared using a 95% solution mixture of FAI (1 M), PbI_2 (1.1 M), MABr (0.2 M), $PbBr_2$ (0.22 M) in DMF : DMSO = 4 : 1 (v : v) and 5% CsI solution (1.5 M) in DMSO. The 150 µL precursor solution was spun on the SnO2/FTO at 1,000 rpm for 10 s, then 6,000 rpm for 20 s in a nitrogen-filled glovebox. During the second step, 500 µL of CB was quickly dripped on the spinning film 5 s prior to the end of the program. Subsequently, the sample was annealed at 100 °C for 1 hour. For the Al_2O_3@HTM, different concentrations of Al_2O_3 NPs (Sigma-Aldrich, cat. no. 702129) dissolved in IPA was coated using a dynamic spin-coating method at 5,000rpm for 40 s before HTM deposition. The Spiro-OMeTAD solution [72.3 mg Spiro-OMeTAD in 1 mL CB with 27.8 µL tBP, 17.8 µL Li-TFSI (520 mg mL^{-1} in AN), and 3 mg FK209] was spin-coated at 5,000 rpm for 30 s. The polymeric HTM in 2MA (15 mg mL^{-1}) was spin-coated on the perovskite at 4,000 rpm for 30 s. The devices were completed by evaporating a gold or silver electrode (80 nm) under high vacuum conditions.

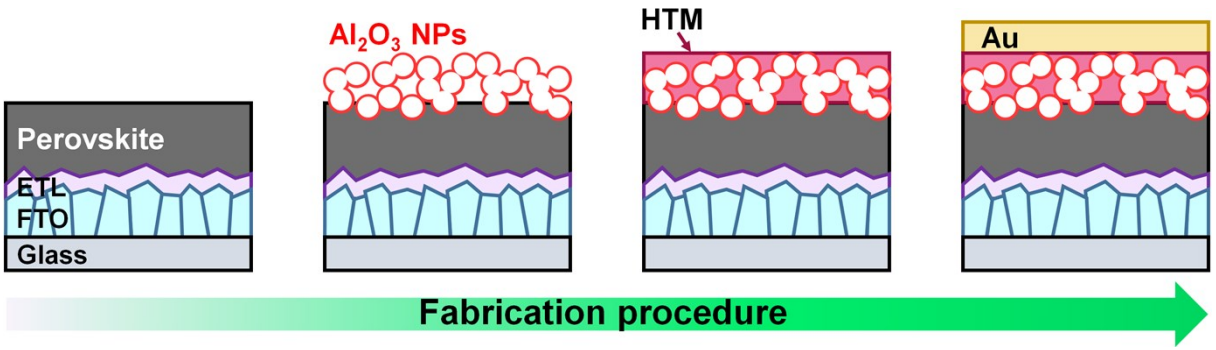

Device characterization

J–*V* characteristics, and maximum power point tracking (MPP) were taken using a Keithley 2400 SMU and an Oriel xenon lamp (450 W) with an AM1.5G filter. The devices were measured in reverse scan (1.2 V to -0.2 V) and forward scan (-0.2 V to 1.2 V) with 0.02 V s^{-1} of scan rate under AM 1.5G illumination of 100 mW cm^{-2} (Oriel 1 kW solar simulator), which was calibrated with a KG5 filter certified by NREL. The active area of the device is 0.09 cm^2, which was determined by the mask placed in front of the device. The MPP was measured at the maximum power point voltage under 1 sun illumination. Space-charge-limited current (SCLC) characteristics of hole-only devices were measured using a Keithley 2400 SMU in forward scan (0 V to 5 V). Incident photon-to-current efficiency (IPCE) measurements were conducted using a constant 100 W Xenon lamp source with an automated monochromator filter. The IPCE measurements were performed in the wavelength range of 300−1100 nm, chopped at 4 Hz (IQE-200B model) with 0.76 mm × 1.0 mm rectangular spot size. A time correlated single photon counting (TCSPC) system (HAMAMATSU/C11367-31) was used for time-resolved photoluminescence (TRPL) analysis. Steady state photoluminescence (PL) measurements were conducted using the high resolution monochromator and hybrid photomultiplier detector (PMA Hybrid 40, PicoQuant GmbH). The top-view and the cross-sectional images of perovskite solar cells were measured using a field emission scanning electron microscope (FE-SEM, Hitachi S 4800). The elemental EDS mapping analysis were obtained by high resolution FE-SEM (HR FE-SEM, JSM 7800F PRIME with Dual EDS). The impedance of devices was analyzed using a computer-controlled potentiostat (SP-200, BioLogic). Surface morphology of samples were investigated by atomic force microscope (AFM) (Digital Instruments Multimode Nanoscope III).

Stability test

For stability measurements, the devices were aged under high temperature and high humidity conditions. All devices for stability tests were stored in dark conditions. Thermal stability tests were performed on a hotplate, demonstrating devices temperature of 85 °C in airtight containers to simulate a real operating environment. To achieve 85% RH, RH was calculated using the ideal gas law and water vapor pressure. Purified water was incorporated in the airtight container to produce RH of 85%. After achieving liquid-gas equivalent, the humidity was adjusted to about 85%.[1,2] *J*–*V* characteristics of the device were periodically measured under AM 1.5G illumination of 100 mW cm^{-2} after cooling down the device to room temperature.

Thermal conductivity analysis

The thermal diffusivities of the HTMs were measured by the time-domain thermoreflectance method (TMX scientific, Transometer™). The square specimens were irradiated with a laser pulse (wavelength: visible, heating energy on sample: 0–50 μJ). The thermal conductivity (κ) was calculated using the equation:

$$\kappa = \alpha \times C_p \times \rho$$

where, α is the thermal diffusivity, C_p and ρ are the heat capacity and density of the HTMs, respectively. The C_p was obtained with differential scanning calorimeter (DSC).

Thermal imaging

The thermal images were taken using a FLIR thermal infrared camera (FLIR System, FLIR E6; sensitivity < 0.06 °C; resolution of 160 × 120 pixels; accuracy ±2% of reading, for ambient temperature and object temperature). Emissivity, a measure of the efficiency of thermal energy emission at the surface, can vary depending on view angle, material, temperature, and roughness. We can adjust the emissivity in the camera settings to reflect the emissivity of the objects. For each photograph taken, Emissivity on all images was set at 0.98 (basic setting) in this study. Images from the IR camera were processed with the respective program (FLIR Tools).

PL analysis

The TRPL and steady-state PL were performed on the prepared samples (glass/perovskite or glass/perovskite/HTM) by a tTCSPC system. The samples were excited using a pulse laser with wavelength of 474nm, fluence of ~ 4 nJ cm^{-2}, a repetition rate of 100 kHz, and a pulse width of 70 ps. The decay constants from the PL data were calculated using the bi-exponential equation:

$$f(t) = A_1 \exp(-\frac{t}{\tau_1}) + A_2 \exp(-\frac{t}{\tau_2}) + y_0$$

where, A is the decay amplitude, and τ is the decay time.

Grazing incidence wide-angle X-ray scattering (GIWAXS) analysis

2D-GIWAXS measurements were performed at a synchrotron radiation on the beam line 3C at the Pohang Accelerator Laboratory (PAL), Korea. All HTMs were spin-coated onto a silicon substrate in the same procedure as the device fabrication. GIWAXS measurements were conducted with a sample-to-detector distance of 212 mm, an X-ray radiation beam energy of 10.26 keV in a vacuum chamber. To monitor the in situ morphological change of HTMs, the sample stage was heated to 150 °C during GIWAXS measurements. All samples were kept for 10 min at each temperature for sufficient morphology change.

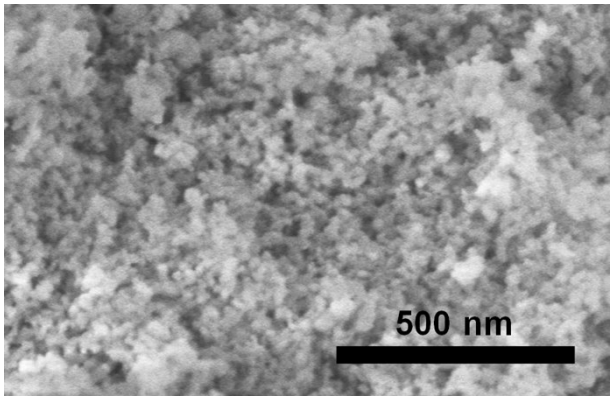

Fig. S1 A top-view SEM image of Al_2O_3 nanoparticles.

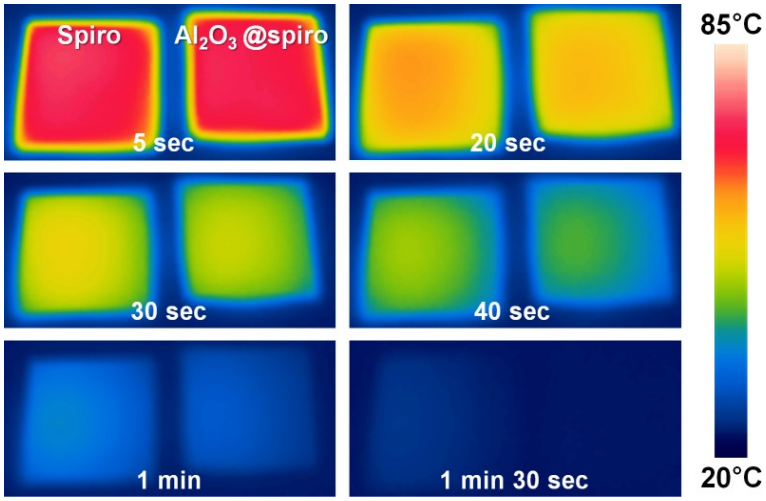

Fig. S2 IR thermal images of conventional HTM (Spiro-OMeTAD) and Al_2O_3@spiro-OMeTAD under a plate-cooling test. All samples were prepared on the perovskite layer.

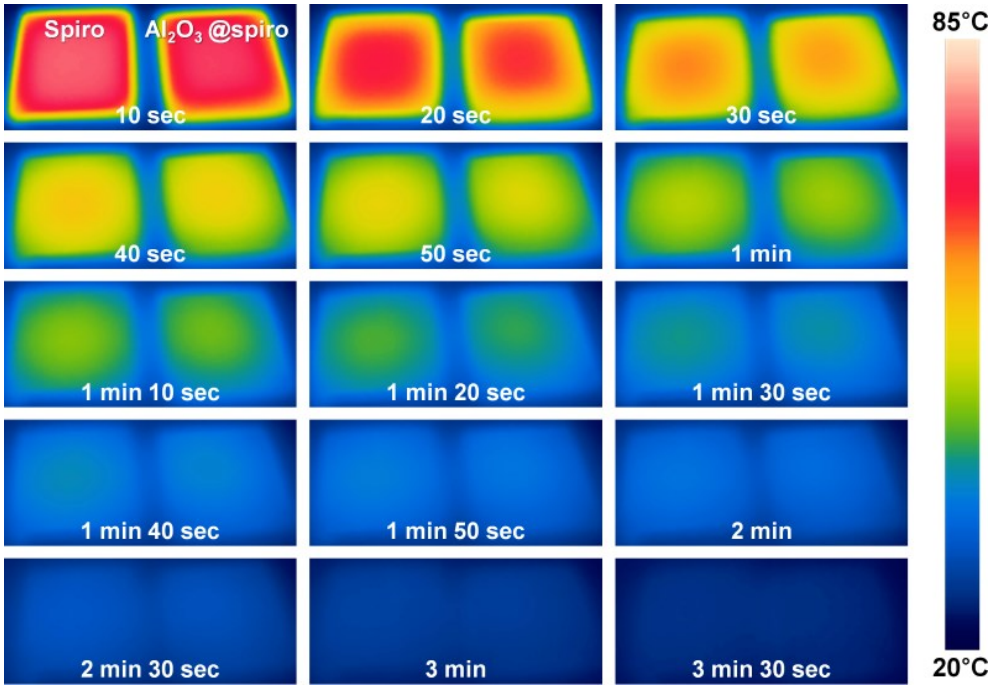

Fig. S3 IR thermal images of conventional HTM (Spiro-OMeTAD) and Al_2O_3@spiro-OMeTAD under the surrounding environment of 20 °C. All samples were prepared on the perovskite layer.

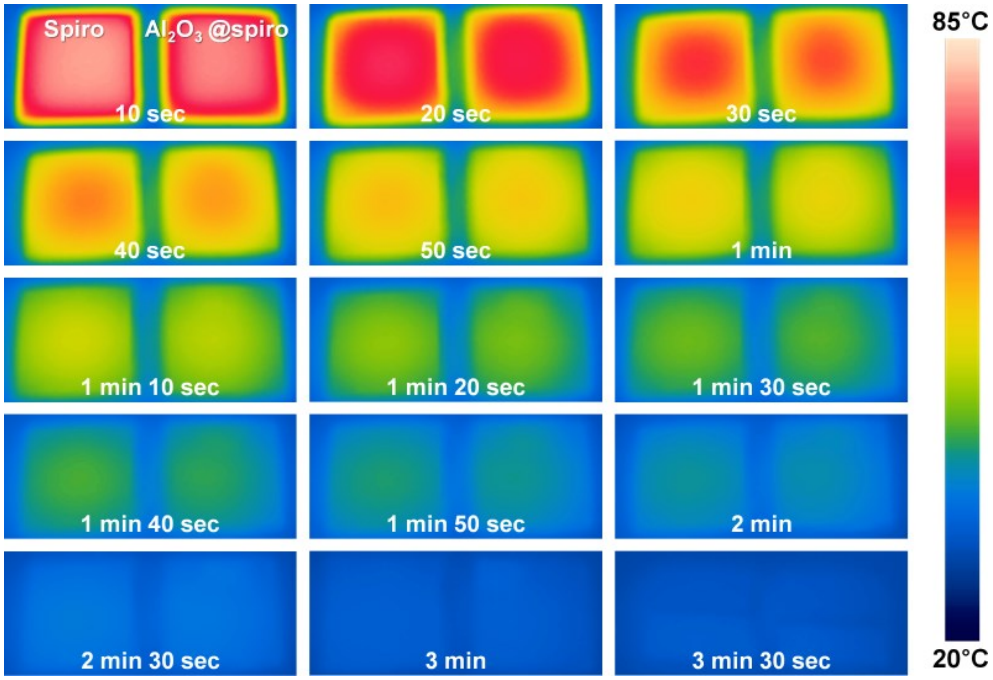

Fig. S4 IR thermal images of conventional HTM (Spiro-OMeTAD) and Al_2O_3@spiro-OMeTAD under the surrounding environment of 30 °C. All samples were prepared on the perovskite layer.

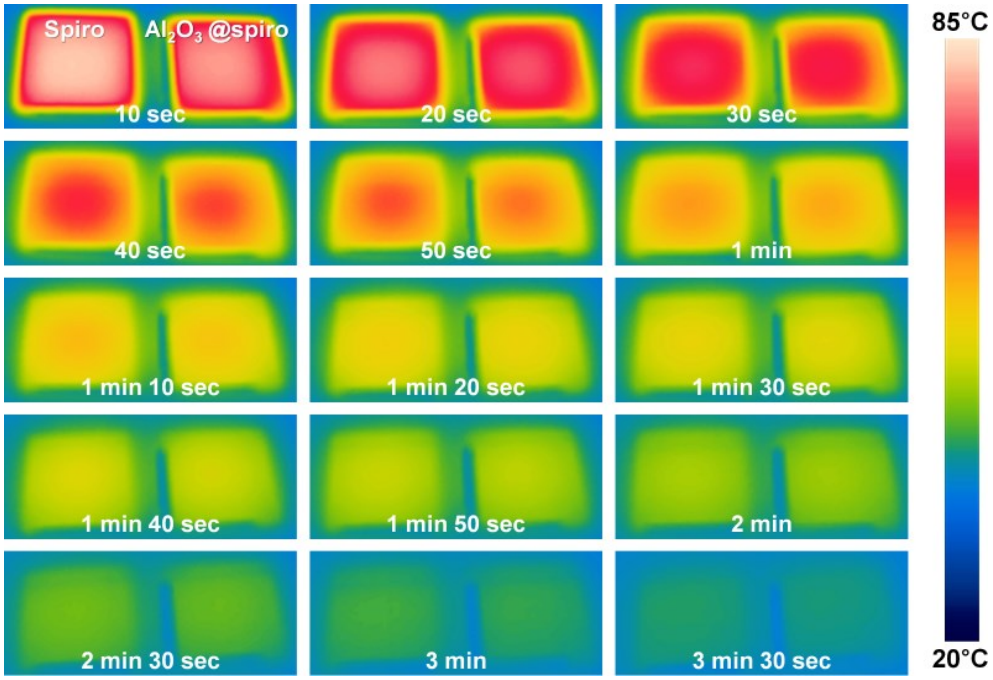

Fig. S5 IR thermal images of conventional HTM (Spiro-OMeTAD) and Al_2O_3@spiro-OMeTAD under the surrounding environment of 40 °C. All samples were prepared on the perovskite layer.

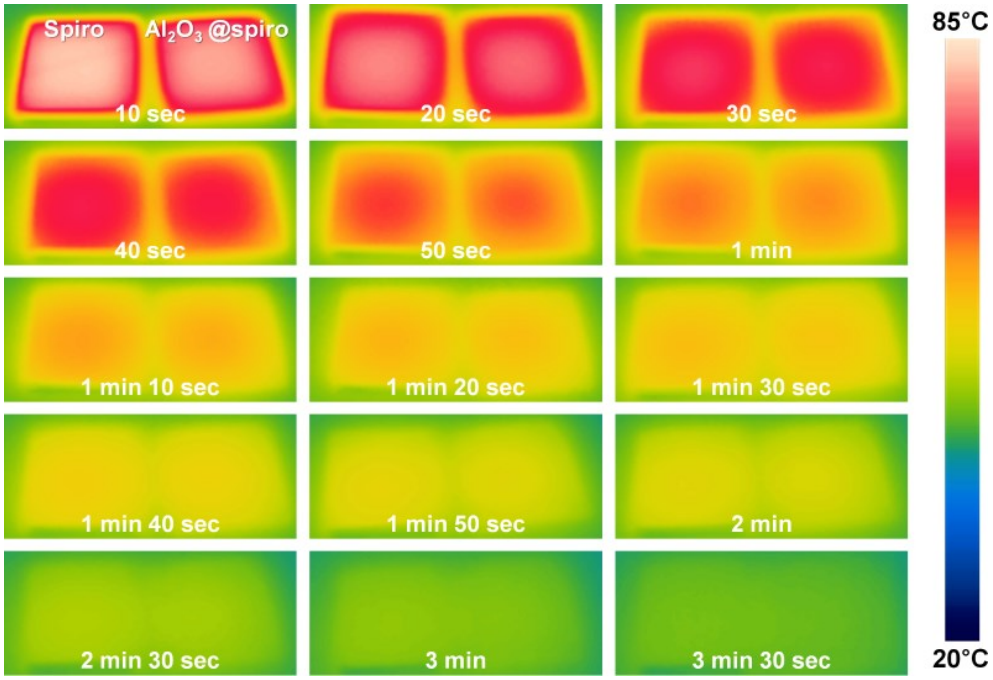

Fig. S6 IR thermal images of conventional HTM (Spiro-OMeTAD) and Al_2O_3@spiro-OMeTAD under the surrounding environment of 50 °C. All samples were prepared on the perovskite layer.

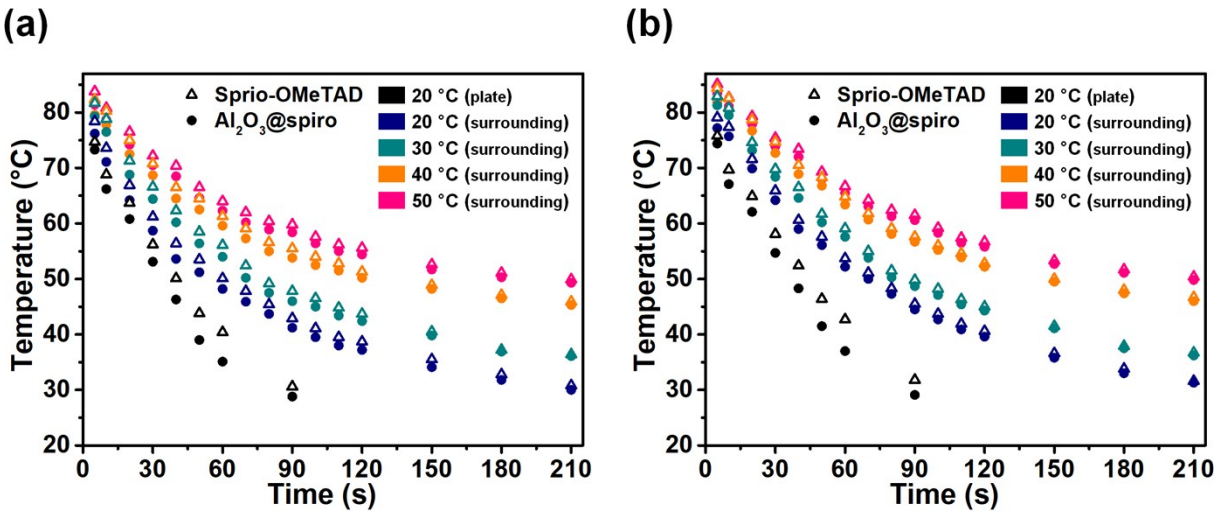

Fig. S7 Transient variation of (a) average and (b) maximum surface temperature under different cooling test conditions.

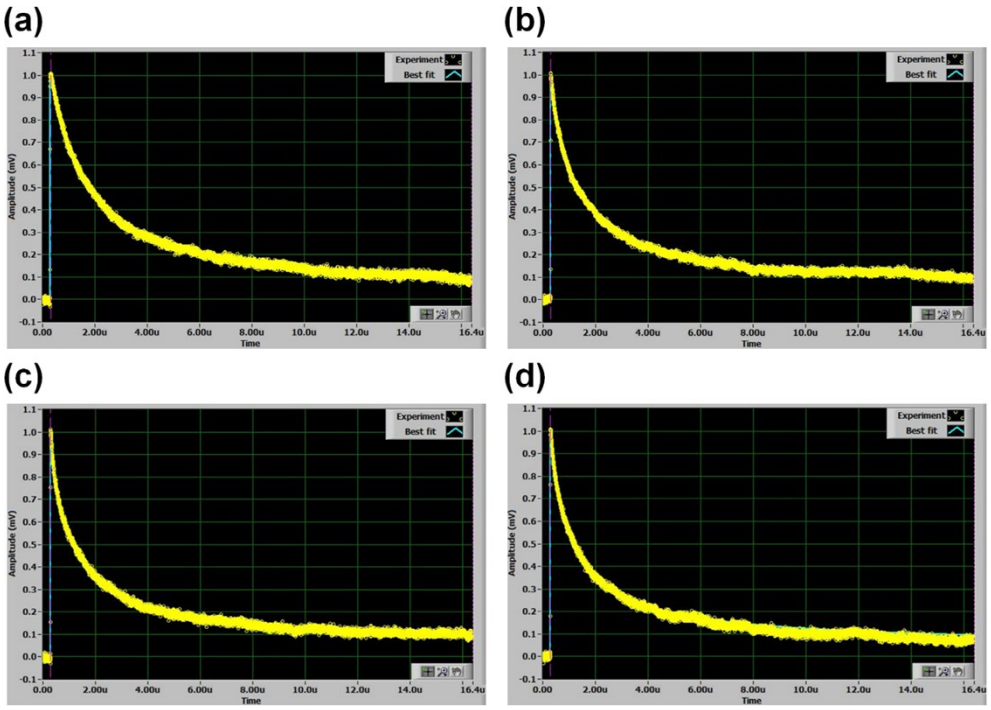

Fig. S8 Thermoreflectance signals of Al_2O_3@spiro-OMeTAD films made using different concentrations of Al_2O_3 NPs ((a) 0, (b) 0.5, (c) 1.0, and (d) 1.5 wt%).

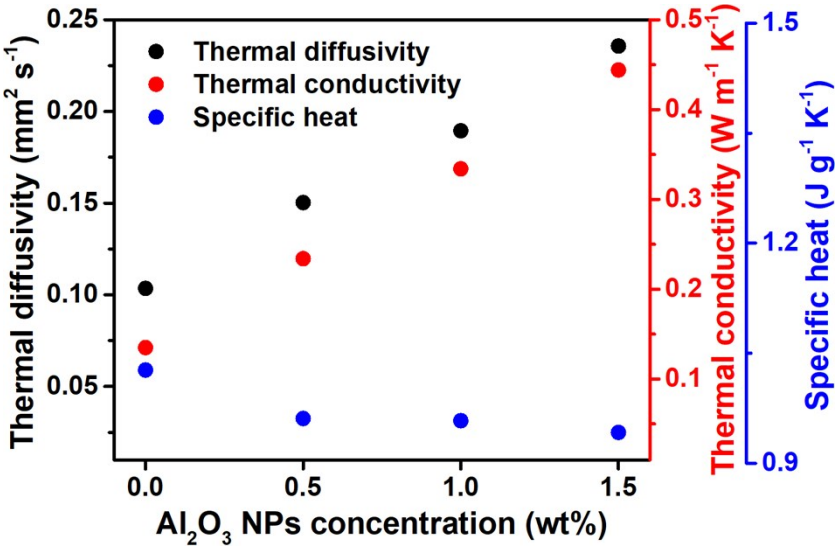

Fig. S9 Thermal diffusivity, thermal conductivity, and specific heat of Al_2O_3@spiro-OMeTAD made using different concentrations of Al_2O_3 NPs.

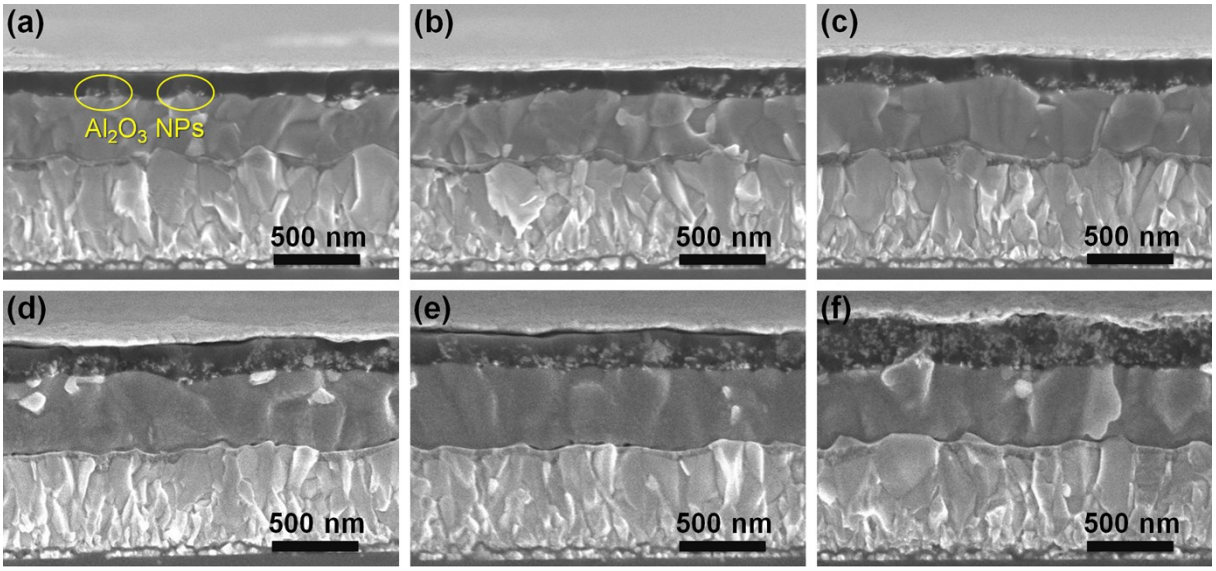

Fig. S10 Cross-sectional SEM images of PSCs with Al_2O_3@spiro-OMeTAD made using different concentrations of Al_2O_3 NPs ((a) 0.3, (b) 0.5, (c) 1.0, (d) 1.5, (e) 2.0, and (f) 4.0 wt%).

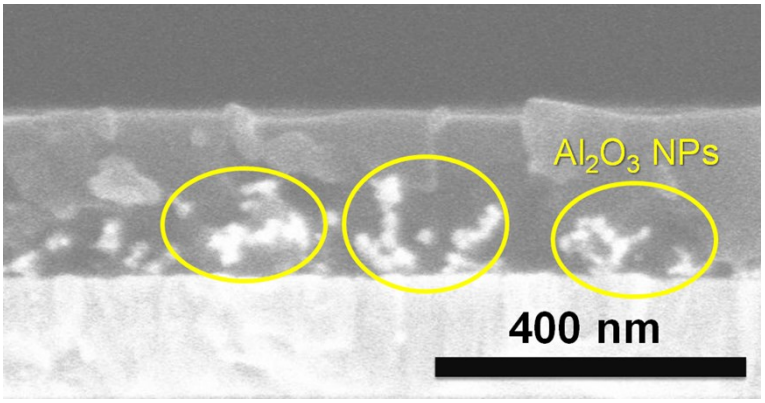

Fig. S11 Cross-sectional SEM image of Al_2O_3 0.3 wt%@spiro-OMeTAD with high magnification. During a high magnification measurement, the perovskite underlayer decomposed and it was difficult to focus. For this reason, a sample was prepared on the ITO substrate without any other layer.

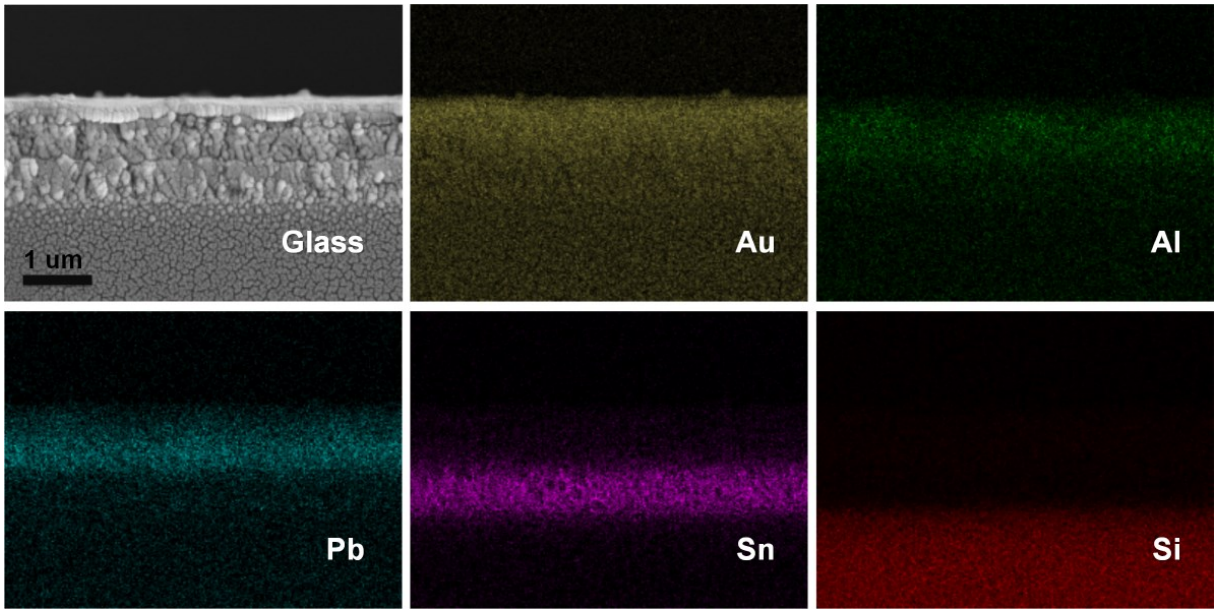

Fig. S12 Cross-sectional elemental mapping images of a PSC using Al_2O_3 0.5 wt%@spiro-OMeTAD.

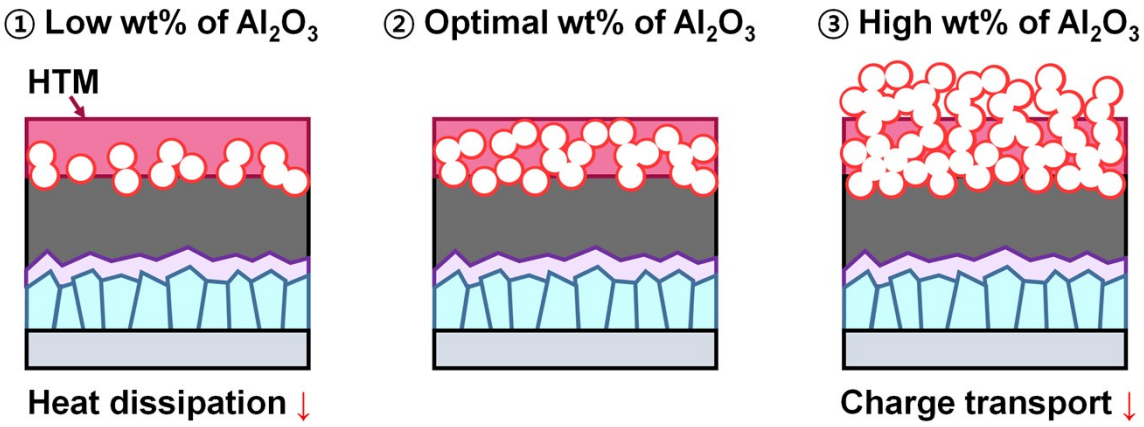

Fig. S13 Schematic illustration of the device structure made using different concentrations of Al_2O_3 NPs.

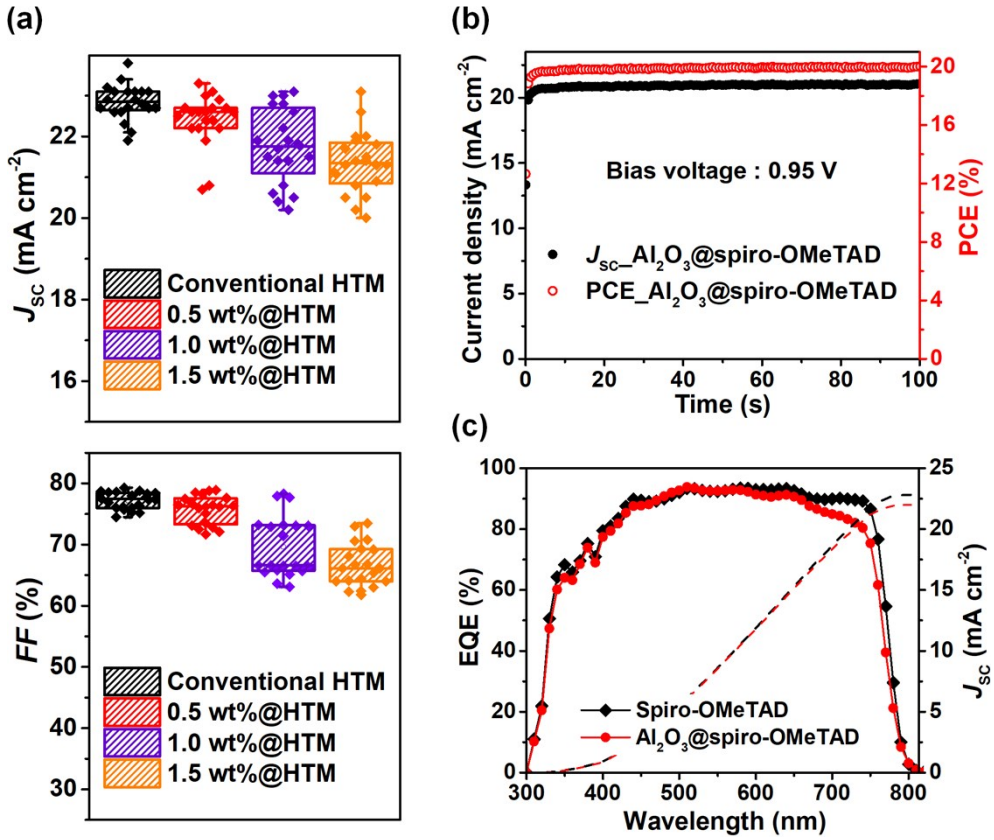

Fig. S14 (a) Device statistics of J_{SC} and FF in PSCs using a conventional HTM (doped Spiro-OMeTAD) with different concentrations of Al_2O_3 NPs. (b) Stabilized power output and current at maximum power point of the champion device as a function of time. (c) EQE spectra of Spiro-OMeTAD and Al_2O_3 0.5 wt%@spiro-OMeTAD based devices.

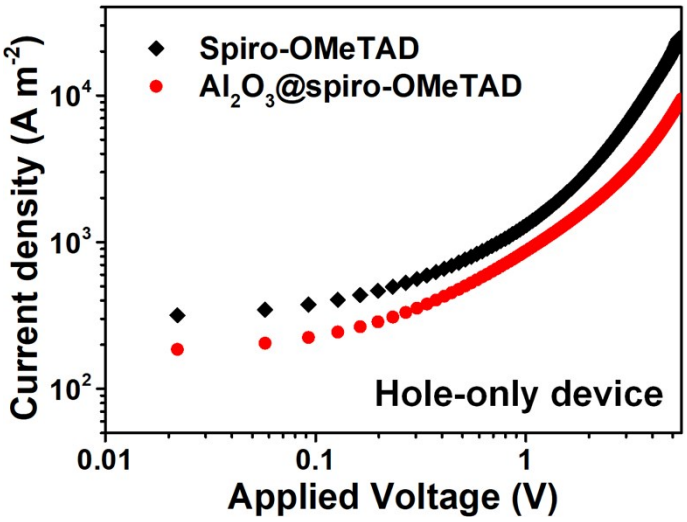

Fig. S15 SCLC characteristics of hole-only devices with Spiro-OMeTAD and Al_2O_3 0.5 wt%@spiro-OMeTAD.

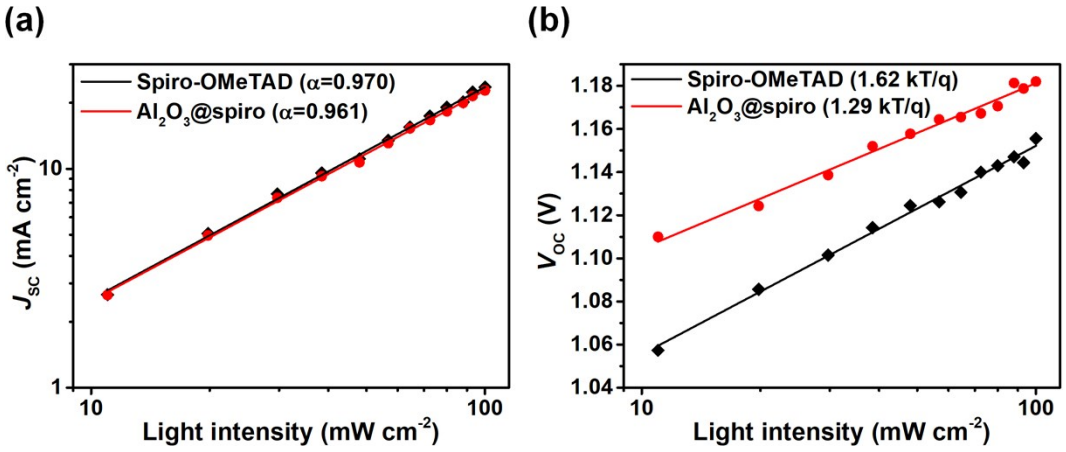

Fig. S16 Light intensity dependence of the (a) J_{SC} and (b) V_{OC}.

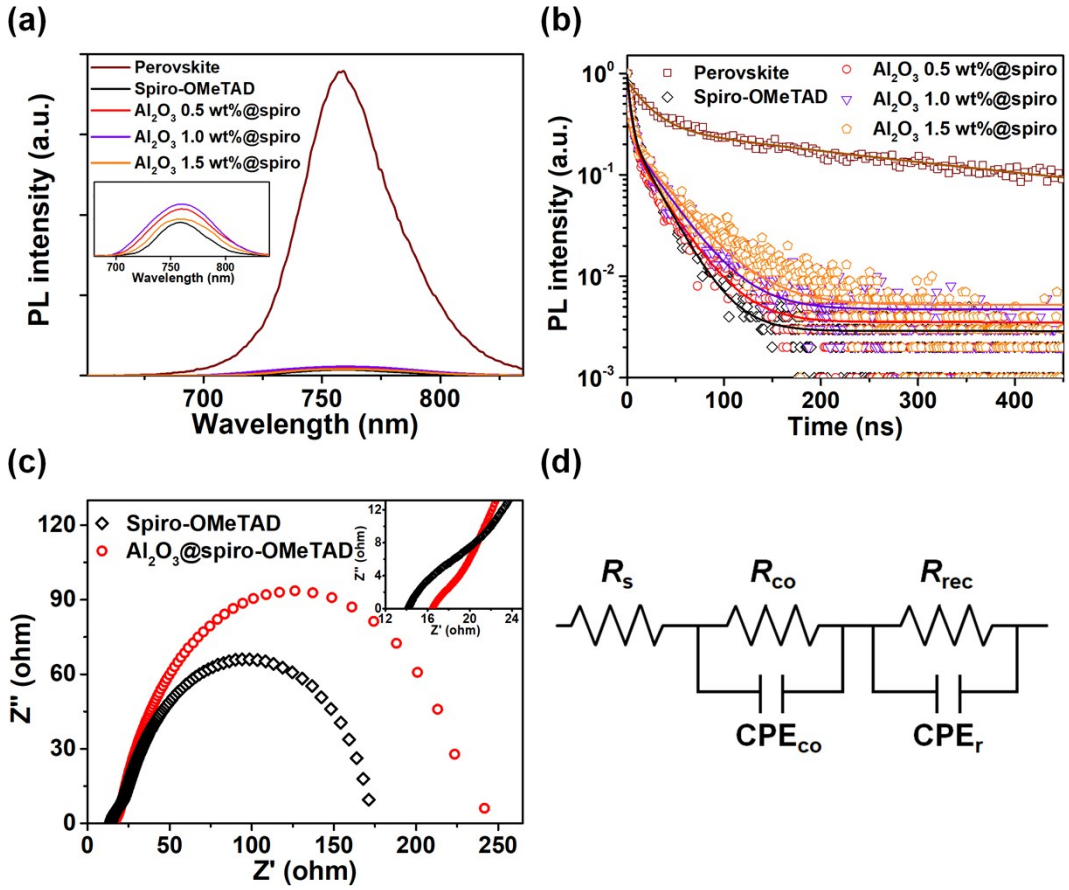

Fig. S17 (a) Steady-state PL and (b) TRPL spectra of samples containing Al_2O_3@spiro-OMeTAD made using different concentrations of Al_2O_3 NPs (inset: the enlarged PL intensity). (c) Nyquist plots of PSCs with Spiro-OMeTAD and Al_2O_3 0.5 wt%@spiro-OMeTAD (inset: the enlarged EIS at the high-frequency region). (d) Equivalent circuit model.

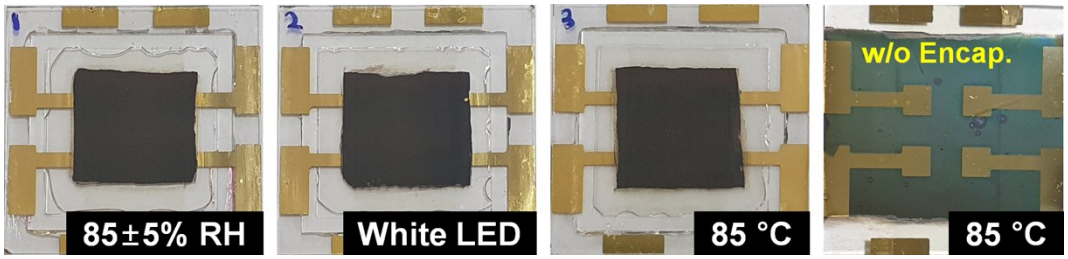

Fig. S18 Photographs of encapsulated devices (perovskite side) and an unencapsulated device (HTM side) after 1000 hours.

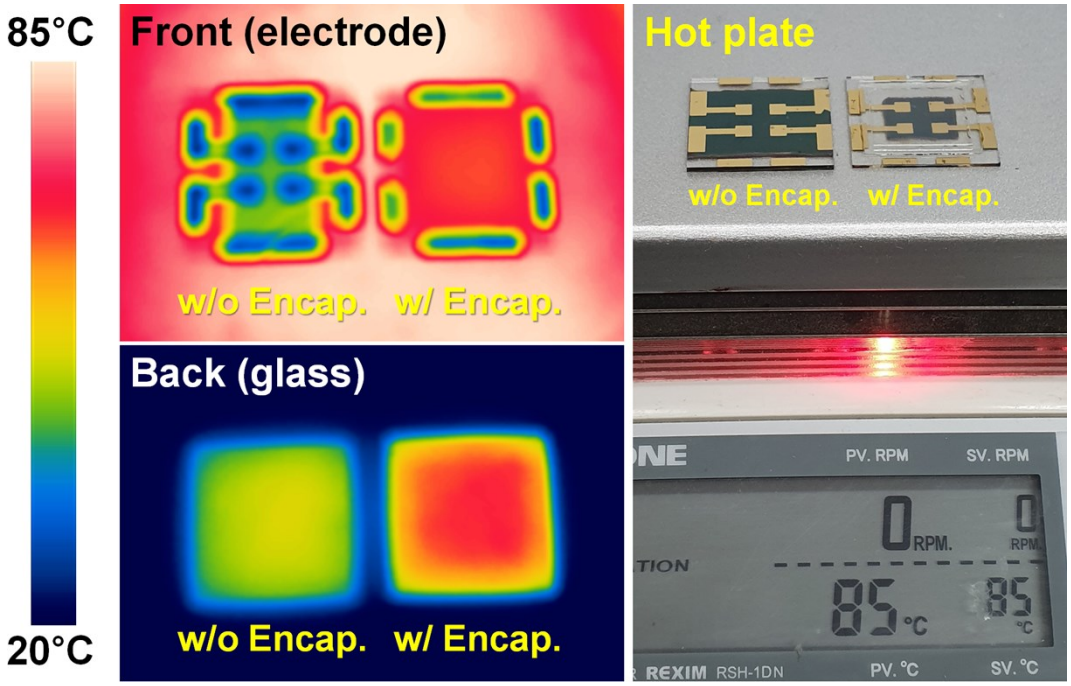

Fig. S19 IR thermal images of devices with and without encapsulation. Both devices were heated on a hotplate at 85 °C. The electrodes have different reflectivity from glass, making it difficult to measure the actual temperature (electrode side); Therefore, after heating devices on a hot plate, we reversed them at the same time and compared the temperature of each device (glass side).

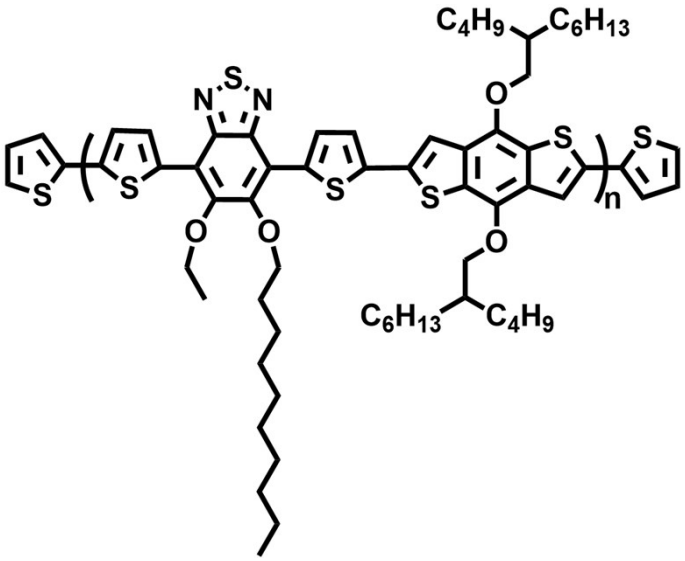

Fig. S20 Chemical structure of a polymeric HTM (Asy-PBTBDT).

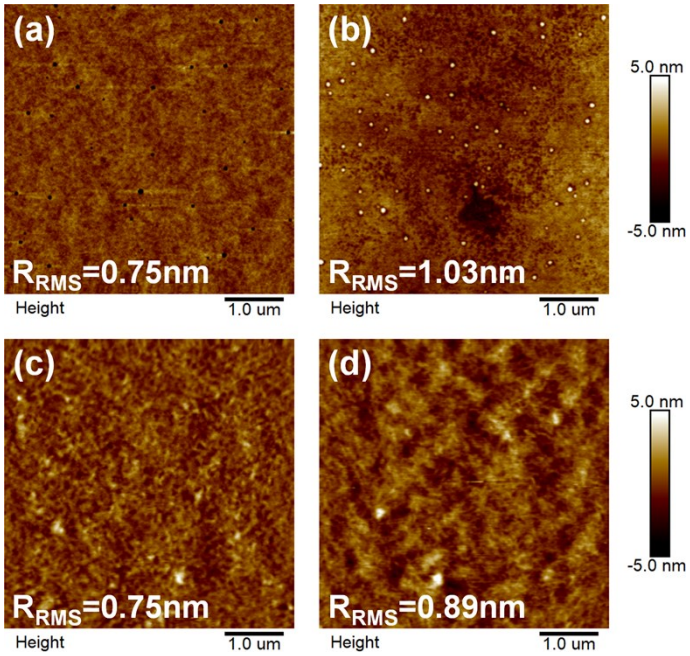

Fig. S21 AFM images of doped Spiro-OMeTAD (a) before and (b) after thermal annealing. AFM images of dopant-free Asy-PBTBDT (c) before and (d) after thermal annealing.

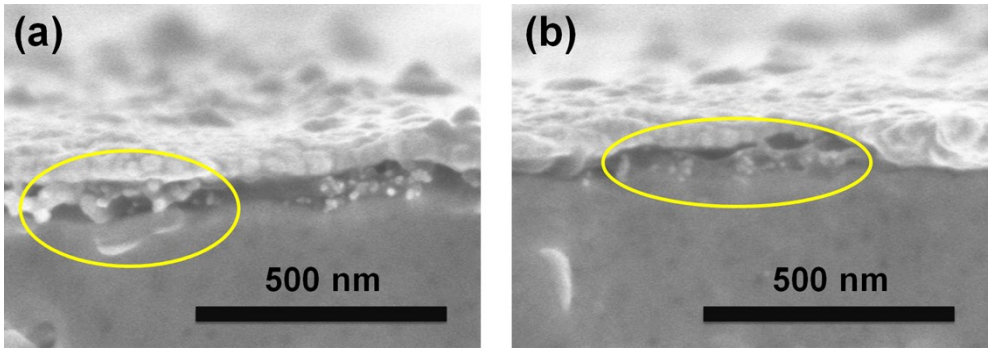

Fig. S22 Cross-sectional SEM images of PSCs with Al_2O_3@asy-PBTBDT made using different concentrations of Al_2O_3 NPs ((a) 0.5 and (b) 0.1 wt%).

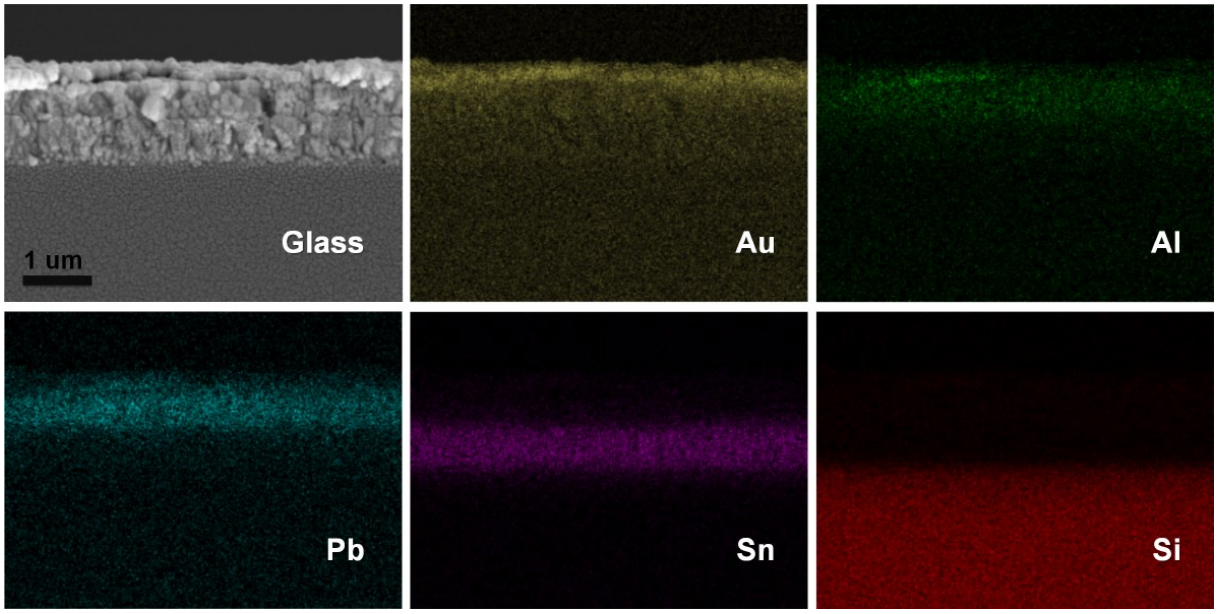

Fig. S23 Cross-sectional elemental mapping images of a PSC using Al_2O_3 0.1 wt%@asy-PBTBDT.

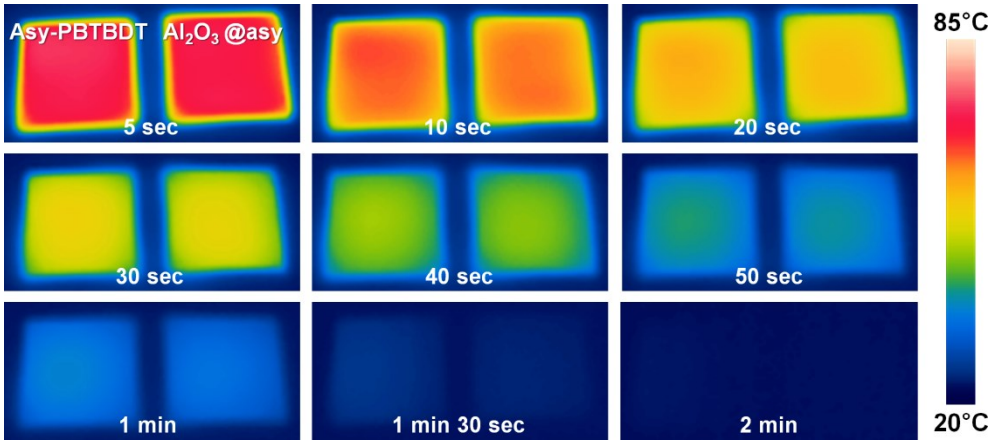

Fig. S24 IR thermal images of polymeric HTM (Asy-PBTBDT) and Al_2O_3@asy-PBTBDT under a plate-cooling test. All samples were prepared on the perovskite layer.

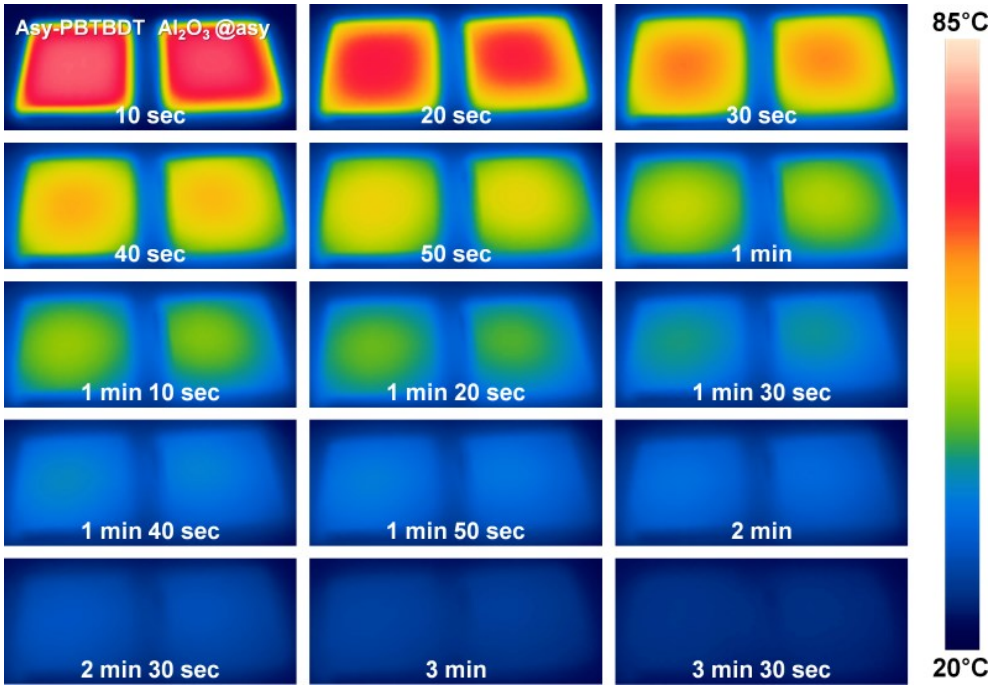

Fig. S25 IR thermal images of polymeric HTM (Asy-PBTBDT) and Al_2O_3@asy-PBTBDT under the surrounding environment of 20 °C. All samples were prepared on the perovskite layer.

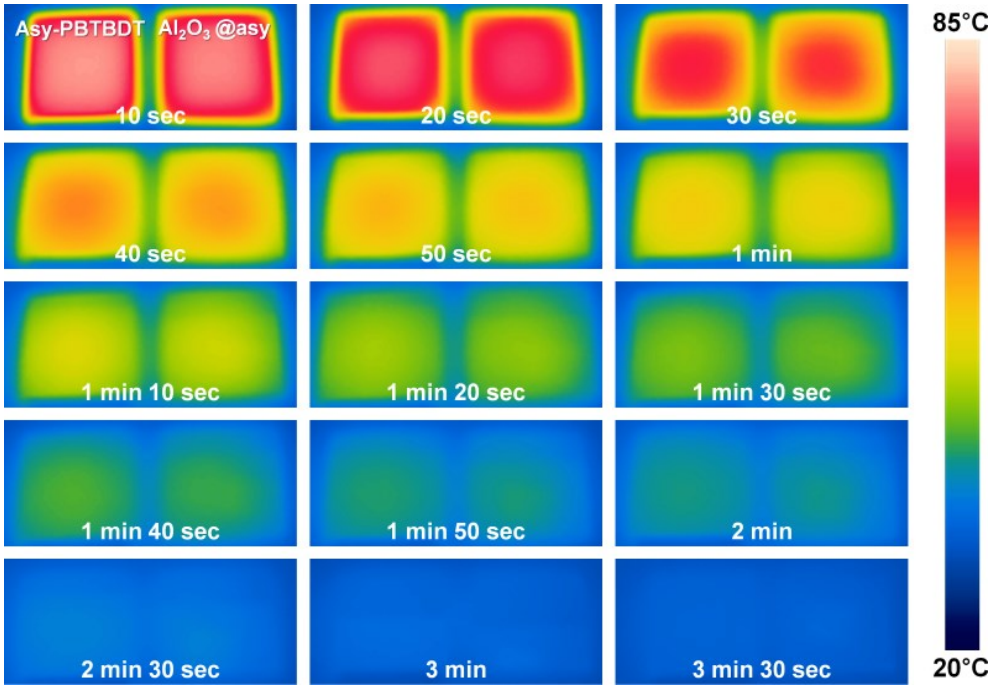

Fig. S26 IR thermal images of polymeric HTM (Asy-PBTBDT) and Al_2O_3@asy-PBTBDT under the surrounding environment of 30 °C. All samples were prepared on the perovskite layer.

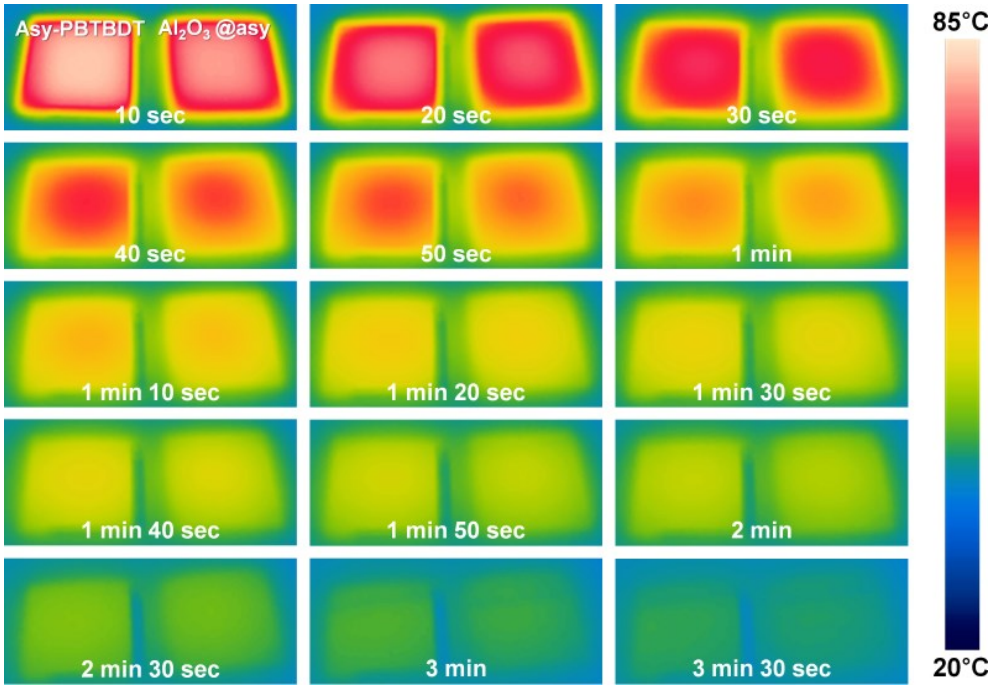

Fig. S27 IR thermal images of polymeric HTM (Asy-PBTBDT) and Al_2O_3@asy-PBTBDT under the surrounding environment of 40 °C. All samples were prepared on the perovskite layer.

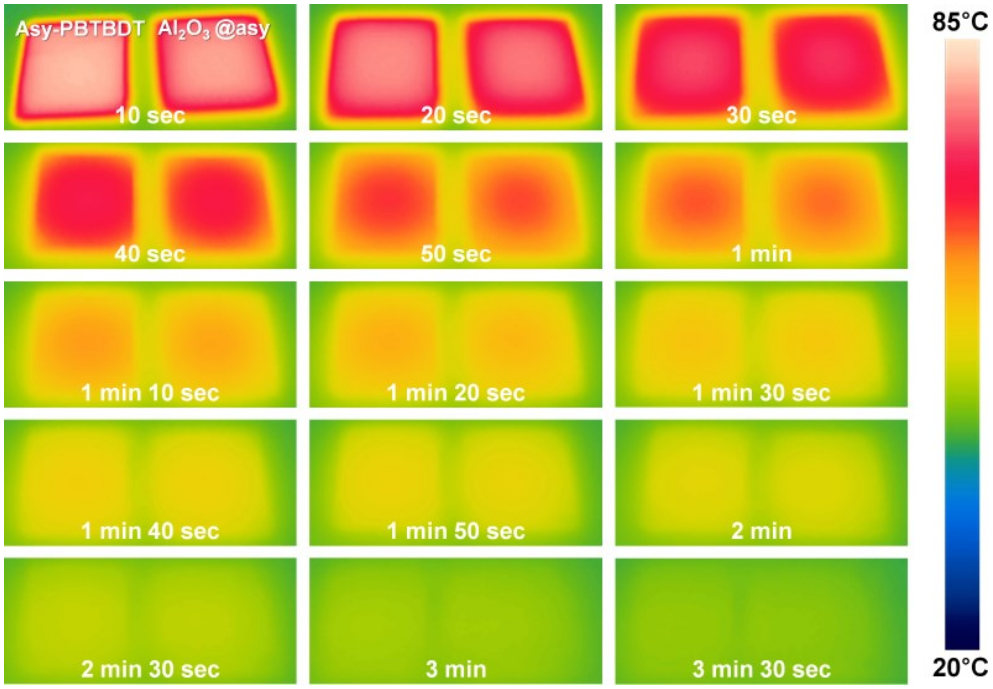

Fig. S28 IR thermal images of polymeric HTM (Asy-PBTBDT) and Al_2O_3@asy-PBTBDT under the surrounding environment of 50 °C. All samples were prepared on the perovskite layer.

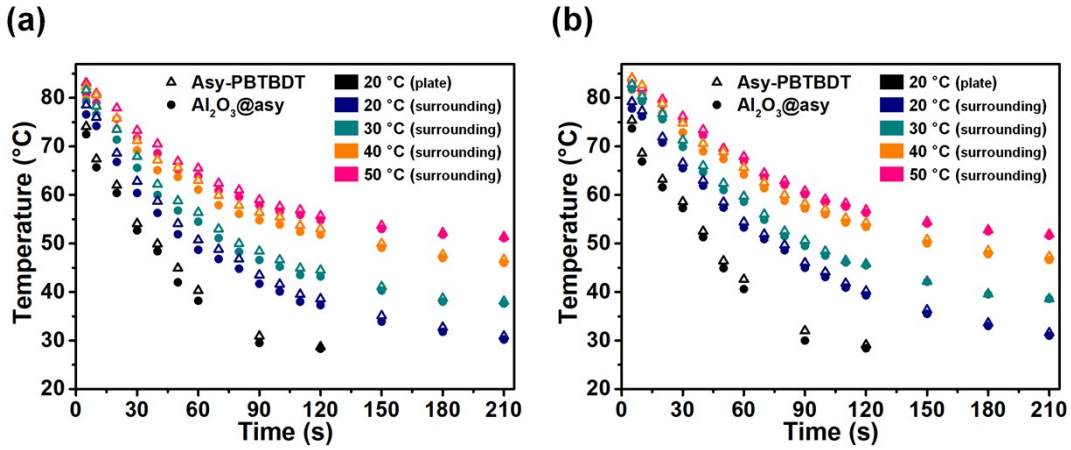

Fig. S29 Transient variation of (a) average and (b) maximum surface temperature under different cooling test conditions.

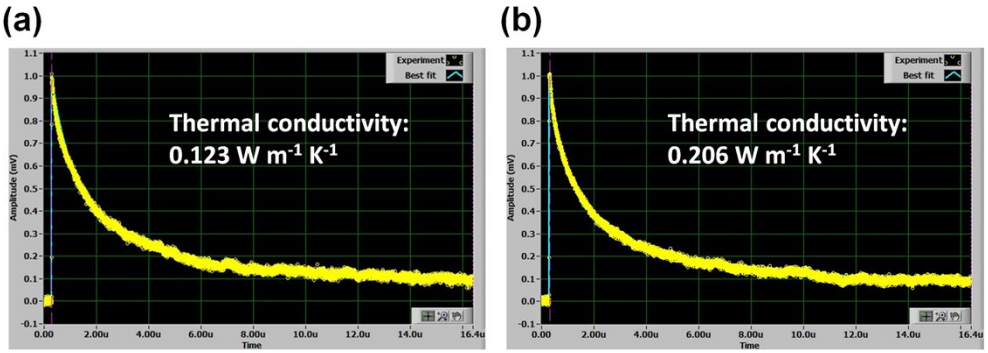

Fig. S30 Thermoreflectance signals and thermal conductivities of (a) Asy-PBTBDT and (b) Al_2O_3 0.1 wt%@asy-PBTBDT films.

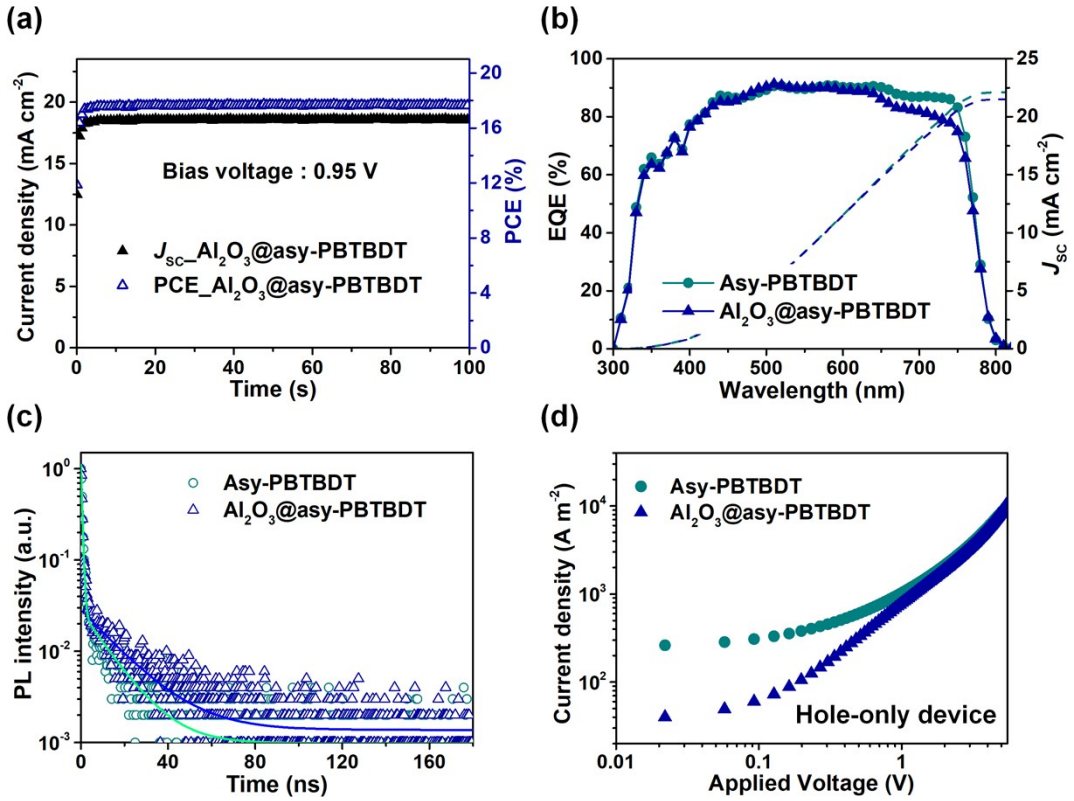

Fig. S31 (a) Stabilized power output and current at maximum power point of the champion device as a function of time. (b) EQE spectra of Asy-PBTBDT and Al_2O_3 0.1 wt%@asy-PBTBDT based devices. (c) TRPL spectra of samples containing Asy-PBTBDT and Al_2O_3@asy-PBTBDT. (d) SCLC characteristics of hole-only devices with Asy-PBTBDT and Al_2O_3 0.1 wt%@asy-PBTBDT.

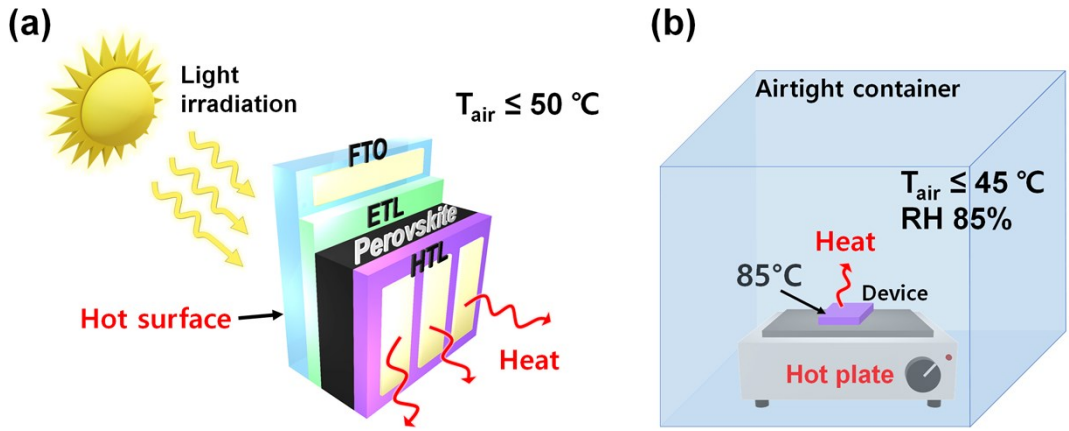

Fig. S32 Schematic illustration of stability test environment. (a) Real operating system of the solar cell and (b) our system.

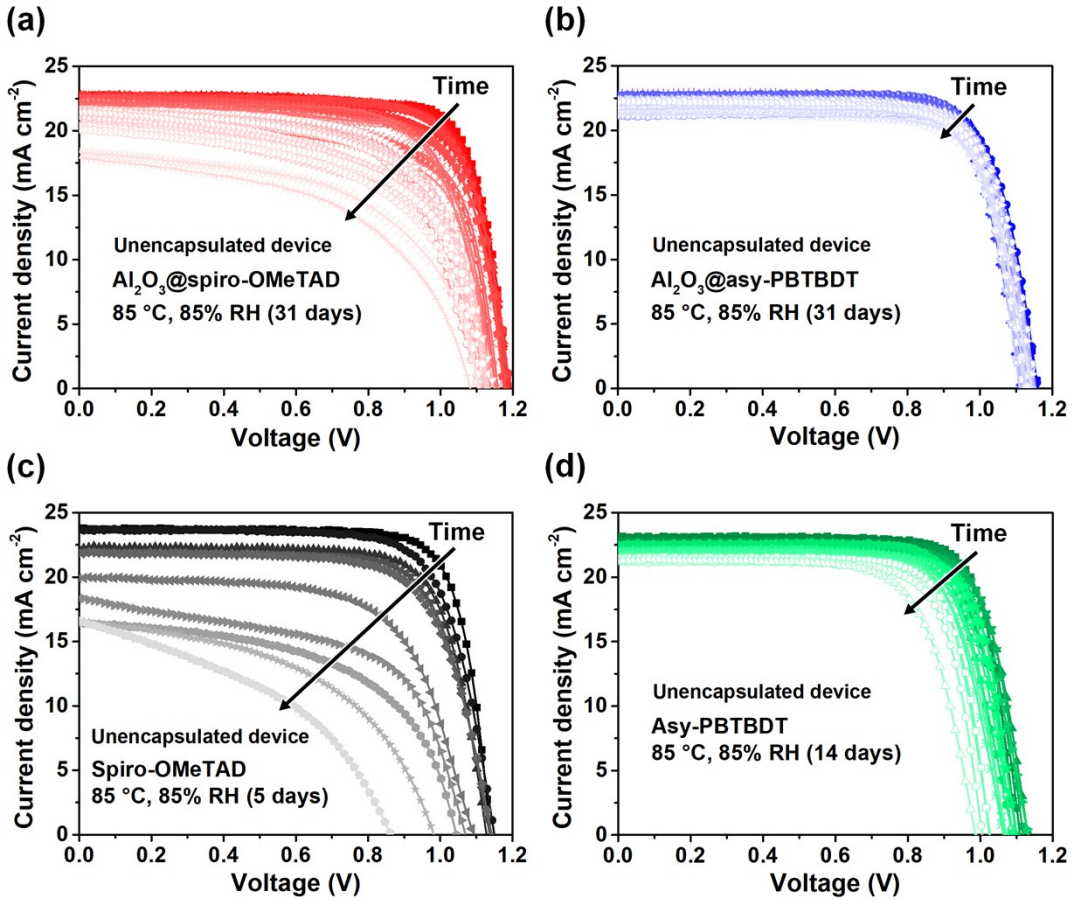

Fig. S33 Stability test duration dependent *J*–*V* curves of the PSC containing (a) Al_2O_3 0.5 wt%@spiro-OMeTAD, (b) Al_2O_3 0.1 wt%@asy-PBTBDT, (c) doped Spiro-OMeTAD, and (d) dopant-free Asy-PBTBDT.

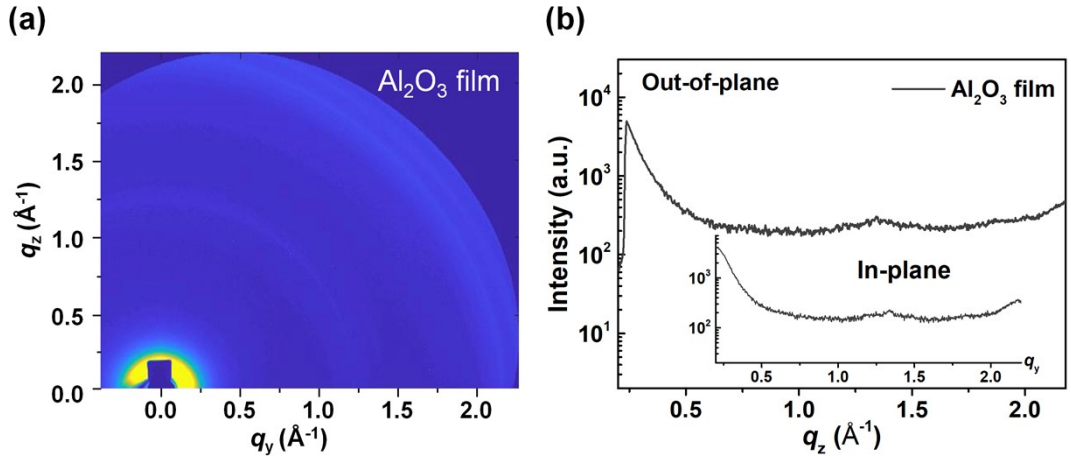

Fig. S34 (a) GIWAXS image of Al_2O_3 layer. (b) GIWAXS intensity profiles of Al_2O_3 along the q_z direction (inset: q_y direction).

Table S1 Summary of fitted decay parameters of Spiro-OMeTAD HTM from TRPL curves.

HTM	τ_1 (ns)	A_1 (%)	τ_2 (ns)	A_2 (%)
Spiro-OMeTAD	3.36	27.5	24.02	72.5
Al_2O_3 0.5 wt%@spiro-OMeTAD	3.65	22.9	28.60	77.1
Al_2O_3 1.0 wt%@spiro-OMeTAD	3.32	27.0	31.04	73.0
Al_2O_3 1.5 wt%@spiro-OMeTAD	3.21	24.1	35.93	75.9

Table S2 Summary of fitted decay parameters of Asy-PBTBDT HTM from TRPL curves.

HTM	τ_1 (ns)	A_1 (%)	τ_2 (ns)	A_2 (%)
Asy-PBTBDT	0.53	97.6	12.27	2.4
Al_2O_3 0.1 wt%@asy-PBTBDT	0.54	97.6	16.58	2.4

Table S3 Stability comparisons of unencapsulated PSCs.

HTM	RH	Temp.*	Testing duration	PCE_i	PCE_f/PCE_i	Reference
Al_2O_3@spiro-OMeTAD	**85%**	**85 °C**	**750 h**	**21.2%**	**54%**	**This work**
Al_2O_3@asy-PBTBDT	**85%**	**85 °C**	**750 h**	**19.9%**	**91%**	**This work**
Spiro-OMeTAD	85%	85 °C	140 h	21.1%	70%	*Energy Environ. Sci.*, 2018, **11**, 3238
Asy-PBTBDT	85%	85 °C	140 h	20.5%	93%	*Energy Environ. Sci.*, 2018, **11**, 3238
Carbon	85%	85 °C	192 h	14.5%	77%	*Adv. Mater.*, 2019, **31**, 1804284
PTAA	55%	85 °C	35 h	18.1%	90%	*Adv. Energy Mater.*, 2018, **8**, 1703421
CuPC	≈30%	85 °C	1100 h	18.8%	97%	*Energy Environ. Sci.*, 2017, **10**, 2109
HTM-free	Air	85 °C	1000 h	16.4%	95%	*Nat. Energy*, 2019, **4**, 939
$CuGaO_2$	N_2	85 °C	1000 h	20.1%	80%	*Adv. Mater.*, 2018, **30**, 1805660
CuPC	25%	150 °C	20 h	14.2%	90%	*Science*, 2019, **366**, 749

PCE_i and PCE_f are the efficiency of devices before and after stability tests, respectively.
*The heat source is not defined in each literature.

Supplementary references

1. J. Lee, T. Kim, S. U. Ryu, K. Choi, G. H. Ahn, J. G. Paik, B. Ryu, T. Park and Y. S. Won, *Sci. Rep.*, 2018, **8**, 11745.
2. Z. Wu, Z. Liu, Z. Hu, Z. Hawash, L. Qiu, Y. Jiang, L. K. Ono and Y. Qi, *Adv. Mater.*, 2019, **31**, 1804284.